Journal of Zhejiang University-SCIENCE A (Applied Physics & Engineering)
ISSN 1673-565X (Print); ISSN 1862-1775 (Online)
www.jzus.zju.edu.cn; www.springerlink.com
E-mail: jzus@zju.edu.cn

# Refined analysis and construction parameter calculation for full-span erection of the continuous steel box girder bridge with long cantilevers*

Jin-feng WANG†, Tian-mei WU, Jiang-tao ZHANG, Hua-wei XIANG, Rong-qiao XU

*College of Civil Engineering and Architecture, Zhejiang University, Hangzhou 310058, China*

†E-mail: wangjinfeng@zju.edu.cn

Received July 9, 2019; Revision accepted Jan. 3, 2020; Crosschecked Mar. 18, 2020

**Abstract:** To accurately control the full-span erection of continuous steel box girder bridges with complex cross-sections and long cantilevers, both the augmented finite element method (A-FEM) and the degenerated plate elements are adopted in this paper. The entire construction process is simulated by the A-FEM with the mesh-separation-based approximation technique, while the degenerated plate elements are constructed based on 3D isoparametric elements, making it suitable for analysis of a thin-walled structure. This method significantly improves computational efficiency by avoiding numerous degrees of freedom (DoFs) when analyzing complex structures. With characteristics of the full-span erection technology, the end-face angle of adjacent girder segments, the preset distance of girder segments from the design position, and the temperature difference are selected as control parameters, and they are calculated through the structural response of each construction stage. Engineering practice shows that the calculation accuracy of A-FEM is verified by field-measured results. It can be applied rapidly and effectively to evaluate the matching state of girder segments and the stress state of bearings as well as the thermal effect during full-span erection.

**Key words:** Continuous steel box girder bridges; Full-span erection; Augmented finite element method (A-FEM); Construction control; Construction parameter calculation

https://doi.org/10.1631/jzus.A1900322 **CLC number:** U445.467

## 1 Introduction

Continuous steel box girder bridges have become the dominant type of long-span bridges because of their large bending stiffness, high torsional rigidity, and good adaptability for rapid construction (Lee et al., 2006; Thang et al., 2009). For the construction of a continuous steel box girder bridge, although the full-span erection technique is high-quality, time-saving, and environmentally friendly, the construction error between the actual geometric shape of a girder and its ideal state of design must be strictly controlled to ensure the quality of deck pavement (Huang, 2007). The long segments of a girder divided in this full-span erection should be accurately positioned to control the construction error of bridge bearings within their allowable eccentricity for installation. Therefore, accurately predicting the deflections and stresses of the girder segments during the entire full-span erection is essential to avoid the influence of geometric errors accumulating as the construction progresses and to control the quality of construction.

For the analysis of continuous steel box girder bridges, beam elements are the most popular used elements. However, there are usually some obvious shear deformations and shear lag effects in a thin-walled steel box girder, and various methods

* Project supported by the National Natural Science Foundation of China (Nos. 51578496 and 51878603) and the Zhejiang Provincial Natural Science Foundation of China (No. LZ16E080001)

ORCID: Jin-feng WANG, https://orcid.org/0000-0002-9099-818x

have been proposed to analyze the impact of these structural behaviors and improve the general applicability of beam elements. Razaqpur and Li (1991) presented a new type of beam element with two end nodes, which included torsional and distortional warping modes, and some additional degrees of freedom (DoFs) were added to allow the occurrence of shear lag effect. However, the additional DoFs depend on the shape of the cross-section, and this restricts the application to some specific cross-sections. Prokić (1993) published a theory for thin-walled beams with arbitrary open or closed cross-section, but the distortion mode was not incorporated in this theory, because the cross-section remained undeformed in its plane. Nguyen et al. (2016) proposed an analytical beam model for a thin-walled, open-section beam made from functionally graded materials. In this beam model, restrained warping was applicable to thin-walled beams, but the shear deformation was not included. These 1D beam elements are usually applied in simulating some simple structures, and cannot comprehensively obtain their geometric and mechanical characteristics. For the analysis of more complex structures, 3D solid or plate elements are more suitable options. However, the computational efficiency with 3D solid or plate elements is much lower than that of the 1D beam elements due to the increase of their DoFs (Liu et al., 2017). To address this problem, Ling et al. (2009) proposed the augmented finite element method (A-FEM) with mesh-separation-based approximation technique, in which the geometrically independent mathematical elements (MEs) and physical elements (PEs) are combined by a specific correlation-rule and applied to construct the approximating function in the mathematical domain and numerically integrate in the physical domain. The A-FEM can describe discontinuous deformation and simulate shear band propagation, and is especially effective in overcoming the mesh sensitivity problem in modeling the standard shear band (Ling et al., 2012). Naderi et al. (2016) extended the A-FEM formulation from 2D to 3D, and proposed a 4-node tetrahedral element, which is a new type of 3D solid element without the need to add DoFs.

Compared with the conventional finite element method (FEM), the spatial A-FEM has proved to be more accurate and efficient in the analysis of complex structures, and thus it was chosen to analyse the entire full-span erection process of a continuous steel box girder bridge in this paper. In this analysis, the degenerated plate elements, created by introducing the assumptions of plate into 3D isoparametric elements, were adopted to comprehensively obtain the geometric and mechanical characteristics of the structure. Based on the A-FEM and degenerated plate elements, the structural responses during the entire long-cantilever full-span erection of a real girder were closely analysed, and some formulae are proposed to determine the construction parameters. Finally, when applied in the actual full-span erection of the Hong Kong-Zhuhai-Macao Bridge, the construction errors during the entire construction were successfully controlled by this method.

## 2 Project background

The Hong Kong-Zhuhai-Macao Bridge is 22.9 km in length, 70% of which is continuous steel box girders with a standard span of 6×110 m (Su and Xie, 2016). The 6×110-m girder adopts a uniform cross-section as displayed in Fig. 1, which is a single-box double-cell steel structure with long cantilevered plates. The division scheme of a 6×110-m girder is shown in Fig. 2, in which the girder is longitudinally divided into six span-scale segments at the locations of zero bending moment. The length of the first segment is 133 m, the final segment is 87 m, and the intermediate four spans are all 110 m. The error of girth-welding should be controlled to less than 2 mm to make the girder segments smoothly connected. In addition, the accumulated construction error during the progress of erection between the actual elevation of bridge deck and its design position is required to be limited within −10 mm to +15 mm. Furthermore, the girder segments must be accurately positioned, and when a girder reaches its ideal state, the eccentricity between the centerlines of the upper bearing plate and lower bearing plate should be controlled within 20 mm.

Owing to the existence of long cantilevers, there is an obvious shear lag effect in the steel girder during full-span erection, and the stress is distributed unevenly along the flanges of the girder (Wu, 2005). Different from the structural performance analyzed

based on elementary beam theory, the normal stresses are non-uniformly distributed along the transverse direction, which will weaken the strength and stiffness of the whole girder (Sapountzakis and Dikaros, 2019). Meanwhile, a non-negligible part of the displacement of the girder is caused by shear deformation (Wu et al., 2002). The cross-section of a girder segment may distort and warp out of the longitudinal plane under an eccentric loading (Vu et al., 2018). In order to comprehensively describe these effects, some mechanical assumptions and complex formulae are needed to be introduced into the beam elements. However, they will greatly affect the accuracy or efficiency of numerical simulation. Therefore, it is important to choose a more appropriate simulation method to achieve high precision control based on the accurate prediction of the deflections and stresses of each construction stage.

## 3 Analytical method

### 3.1 Theory of A-FEM

Different from FEM, two kinds of elements, namely, MEs and PEs, are defined in the A-FEM to geometrically separate the elements for constructing the approximation and those for numerical integration (Fang et al., 2011; Liu et al., 2013; Ling et al., 2014; Jung et al., 2016). MEs are geometric areas for building the displacement mode of elements, while PEs are real physical domains occupied by the structure. As shown in Fig. 3, a physical region can be composed of different materials, such as concrete and steel. We establish a local orthogonal coordinate system $\xi'\eta'\zeta'$ in each PE, and each $\zeta'$ axis is taken as the normal direction of the PE.

The displacement interpolation function defined on the ME, $\boldsymbol{u}$, can be obtained by applying isoparametric interpolation:

$$\boldsymbol{u}=\sum_{i=1}^{n}N_i(\xi,\eta,\zeta)\boldsymbol{d}_i, \tag{1}$$

where $N_i$ is the shape function for displacement interpolation of the MEs, $(\xi, \eta, \zeta)$ is the natural coordinate in the reference element of the MEs, $\boldsymbol{d}_i$ is the displacement vector of the MEs, and $n$ is the node number of the MEs.

Appropriately expanding the definition domain of Eq. (1) to cover the PEs, the displacement interpolation function of the PEs, $\boldsymbol{u}'$, can be derived as

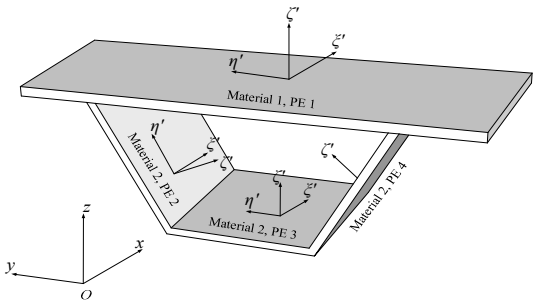


**Fig. 3 Partition of the PEs**

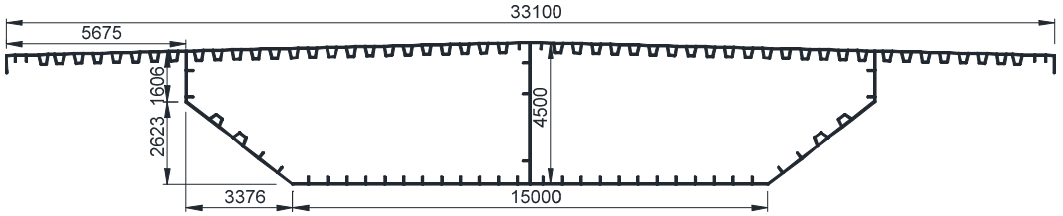


**Fig. 1 Standard cross-section (unit: mm)**

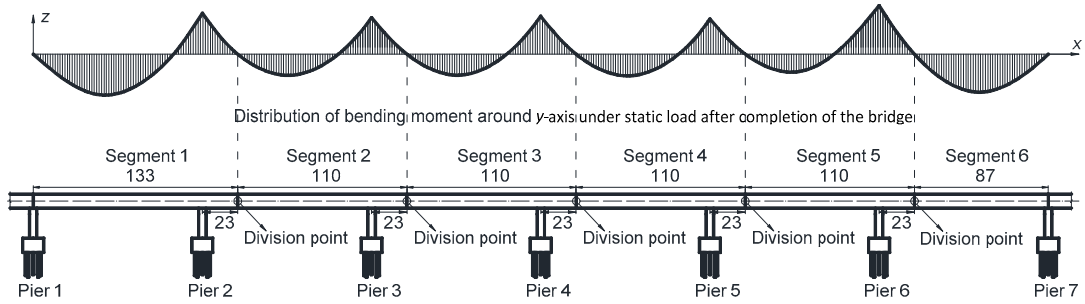


**Fig. 2 Longitudinal division scheme of the girder (unit: m)**

$$\boldsymbol{u}'=\sum_{i=1}^{n}N_i'(\xi,\eta,\zeta)\boldsymbol{d}_i=\boldsymbol{T}\sum_{i=1}^{n}N_i(\xi,\eta,\zeta)\boldsymbol{d}_i, \quad (2)$$

where $N_i'$ is the shape function for displacement interpolation of the PEs, and $\boldsymbol{T}$ is the mapping matrix determined by the deformation characteristic of the PEs (Ling et al., 2014).

The relationship between strain $\boldsymbol{\varepsilon}$ and displacement $\boldsymbol{d}$ in global coordinates is expressed by matrix $\boldsymbol{B}$ as

$$\boldsymbol{\varepsilon}=\boldsymbol{B}\boldsymbol{d}=\begin{bmatrix}\boldsymbol{B}_1 & \boldsymbol{B}_2 & \dots & \boldsymbol{B}_n\end{bmatrix}\begin{bmatrix}\boldsymbol{d}_1^{\mathrm{T}} & \boldsymbol{d}_2^{\mathrm{T}} & \dots & \boldsymbol{d}_n^{\mathrm{T}}\end{bmatrix}^{\mathrm{T}}, \quad (3)$$

$$\boldsymbol{B}_i=\begin{bmatrix}\dfrac{\partial N_i}{\partial x} & 0 & 0 & 0 & \dfrac{\partial N_i}{\partial z} & \dfrac{\partial N_i}{\partial y}\\ 0 & \dfrac{\partial N_i}{\partial y} & 0 & \dfrac{\partial N_i}{\partial z} & 0 & \dfrac{\partial N_i}{\partial x}\\ 0 & 0 & \dfrac{\partial N_i}{\partial z} & \dfrac{\partial N_i}{\partial y} & \dfrac{\partial N_i}{\partial x} & 0\end{bmatrix}^{\mathrm{T}}, \ i=1,2,\dots,n. \quad (4)$$

The fundamental assumptions of degenerated plate elements are the same as those of classical plate theory considering shear deformations, but are not that complicated mathematically. The constitutive relation of different types of components is defined by the modified elastic matrix $\boldsymbol{D}_r'$.

$$\boldsymbol{D}_r'=\frac{E}{1-v^2}\begin{bmatrix}1 & v & 0 & 0 & 0 & 0\\ & 1 & 0 & 0 & 0 & 0\\ & & \lambda & 0 & 0 & 0\\ & & & \dfrac{1-v}{2} & 0 & 0\\ & & \text{symm} & & \dfrac{1-v}{2} & 0\\ & & & & & \dfrac{1-v}{2}\end{bmatrix}, \quad (5)$$

where $E$ is Young's modulus, and $v$ is Poisson's ratio. $\lambda$ is an introduced penalty coefficient, taking zero or a small number when calculating stress, so that the stress perpendicular to the mid-surface of the plate is zero; taking a large number when calculating stiffness, so that the relative deflection of the corresponding point is zero. In this way, the fundamental assumption of the plate is satisfied.

The normal direction of each partitioned plate unit is generally inconsistent with the global coordinates, so $\boldsymbol{D}_r$ is obtained by coordinate transformation.

$$\boldsymbol{D}_r=\boldsymbol{T}_\varepsilon^{\mathrm{T}}\boldsymbol{D}_r'\boldsymbol{T}_\varepsilon, \quad (6)$$

where $\boldsymbol{T}_\varepsilon$ is given as Eq. (7) at the bottom of this page.

In Eq. (7), $l_{\xi'}$, $l_{\eta'}$, $l_{\zeta'}$, $m_{\xi'}$, $m_{\eta'}$, $m_{\zeta'}$, $n_{\xi'}$, $n_{\eta'}$, and $n_{\zeta'}$ are the direction cosines of $\xi'$, $\eta'$, and $\zeta'$ axes relative to the $x$, $y$, and $z$ axes, respectively.

Considering that only the PEs contribute to the virtual work equation and utilizing the coordinate transformation, the elemental stiffness matrix can be written as

$$\boldsymbol{K}=\sum_{r=1}^{s}\int_{-1}^{1}\int_{-1}^{1}\int_{-1}^{1}\boldsymbol{B}^{\mathrm{T}}\boldsymbol{D}_r\boldsymbol{B}\left|\boldsymbol{J}\right|\left|\boldsymbol{J}_r'\right|\mathrm{d}\xi'\mathrm{d}\eta'\mathrm{d}\zeta', \quad (8)$$

$$\boldsymbol{J}=\begin{bmatrix}x_\xi & y_\xi & z_\xi\\ x_\eta & y_\eta & z_\eta\\ x_\zeta & y_\zeta & z_\zeta\end{bmatrix}, \ \boldsymbol{J}_r'=\begin{bmatrix}\xi_{\xi'} & \eta_{\xi'} & \zeta_{\xi'}\\ \xi_{\eta'} & \eta_{\eta'} & \zeta_{\eta'}\\ \xi_{\zeta'} & \eta_{\zeta'} & \zeta_{\zeta'}\end{bmatrix}, \quad (9)$$

where $s$ is the total number of physical regions inside the MEs, $\boldsymbol{J}$ is the Jacobi matrix corresponding to the transformation between the global coordinate and local coordinate of MEs, and $\boldsymbol{J}_r'$ is the Jacobi matrix corresponding to the coordinate transformation between the $r$th PE and its reference element, in which $n_r'$ is the node number of the $r$th PE, and

$$\boldsymbol{T}_\varepsilon=\begin{bmatrix}l_{\xi'}^2 & m_{\xi'}^2 & n_{\xi'}^2 & m_{\xi'}n_{\xi'} & n_{\xi'}l_{\xi'} & l_{\xi'}m_{\xi'}\\ l_{\eta'}^2 & m_{\eta'}^2 & n_{\eta'}^2 & m_{\eta'}n_{\eta'} & n_{\eta'}l_{\eta'} & l_{\eta'}m_{\eta'}\\ l_{\zeta'}^2 & m_{\zeta'}^2 & n_{\zeta'}^2 & m_{\zeta'}n_{\zeta'} & n_{\zeta'}l_{\zeta'} & l_{\zeta'}m_{\zeta'}\\ 2l_{\eta'}l_{\zeta'} & 2m_{\eta'}m_{\zeta'} & 2n_{\eta'}n_{\zeta'} & m_{\eta'}n_{\zeta'}+m_{\zeta'}n_{\eta'} & n_{\eta'}l_{\zeta'}+n_{\zeta'}l_{\eta'} & l_{\eta'}m_{\zeta'}+l_{\zeta'}m_{\eta'}\\ 2l_{\xi'}l_{\zeta'} & 2m_{\xi'}m_{\zeta'} & 2n_{\xi'}n_{\zeta'} & m_{\xi'}n_{\zeta'}+m_{\zeta'}n_{\xi'} & n_{\xi'}l_{\zeta'}+n_{\zeta'}l_{\xi'} & l_{\xi'}m_{\zeta'}+l_{\zeta'}m_{\xi'}\\ 2l_{\xi'}l_{\eta'} & 2m_{\xi'}m_{\eta'} & 2n_{\xi'}n_{\eta'} & m_{\xi'}n_{\eta'}+m_{\eta'}n_{\xi'} & n_{\xi'}l_{\eta'}+n_{\eta'}l_{\xi'} & l_{\xi'}m_{\eta'}+l_{\eta'}m_{\xi'}\end{bmatrix}, \quad (7)$$

$$x_\xi = \sum_{i=1}^{n} \frac{\partial N_i}{\partial \xi} x_i, \quad y_\xi = \sum_{i=1}^{n} \frac{\partial N_i}{\partial \xi} y_i,$$

$$z_\xi = \sum_{i=1}^{n} \frac{\partial N_i}{\partial \xi} z_i, \quad \xi_{\xi'} = \sum_{i=1}^{n'_r} \frac{\partial N_i}{\partial \xi'} \xi_i,$$

$$\eta_{\xi'} = \sum_{i=1}^{n'_r} \frac{\partial N_i}{\partial \xi'} \eta_i, \quad \zeta_{\xi'} = \sum_{i=1}^{n'_r} \frac{\partial N_i}{\partial \xi'} \zeta_i.$$

Because the generation of the mathematical mesh is not strictly dependent on the physical area, not only can the mathematical nodes be defined outside the complex physical boundary, but also the MEs are maintained in an acceptable geometric form. Consequently, the problem of easily distorting on a complex boundary, which is often encountered in FEM, is overcome by A-FEM. Subsequently, different from conventional elements, the shape of PEs is no longer limited to regular triangles or quadrilaterals. Even if there were a hollow region, it can be regarded as an independent region and $\boldsymbol{D}_r$ is zero. Therefore, the constraints for the generations of PEs, including complex boundaries and composition of materials, are removed by A-FEM.

### 3.2 Analysis model

The division for the MEs of the standard cross-section of 6×110-m continuous steel box girder is shown in Fig. 4. The MEs are 20-node 3D isoparametric elements. The structure is divided into one single unit along the vertical direction, 15 units along the longitudinal direction, and seven units along the transverse direction considering the effects of shear lag. The total numbers of mathematical nodes and elements are 848 and 105, respectively. Inside the ME, each plate included in the top plate, bottom plate, web, and stiffeners constitutes one single physical region. The total numbers of physical nodes and elements are 44 619 and 23 040, respectively. The 3D A-FEM model is displayed in Fig. 5.

In order to analyze the effect of the numbers of MEs on the convergence of A-FEM, the vertical deflections and longitudinal normal stress at the mid span are calculated with the increase in the numbers of elements along the longitudinal direction, which are illustrated in Fig. 6.

The results illustrate that when the number of longitudinal elements reaches 15, the deflections and stress are rather close to the refined results, and almost remain stable with more elements. Therefore, the convergence of A-FEM along the longitudinal direction is acceptable in the proposed model.

### 3.3 Method validation

Subjected to the most adverse loading, the first segment of the proposed girder is selected to verify the accuracy of A-FEM for analyzing complex, long-span structures. To compare with the results of the A-FEM model, another two conventional FEM models are also created with the plate elements and beam elements, respectively. Taking the plate element model as an example, as displayed in Fig. 7, it has a total number of 243 963 elements and 198 802 nodes.

The results of the A-FEM, conventional plate elements, beam elements, and the field-measured data after erecting the first segment are provided in Figs. 8 and 9. The results of the maximum deflections and stresses are listed in Table 1.

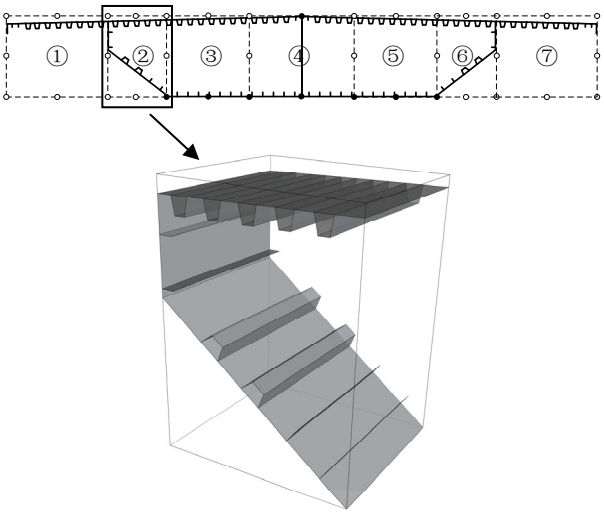


**Fig. 4 Division for MEs of the standard cross-section**

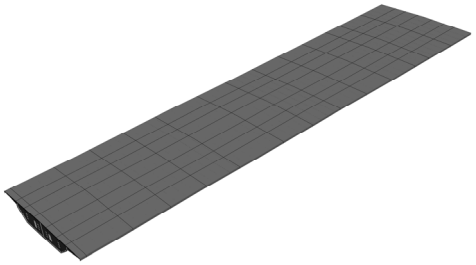

**Fig. 5 A-FEM model**

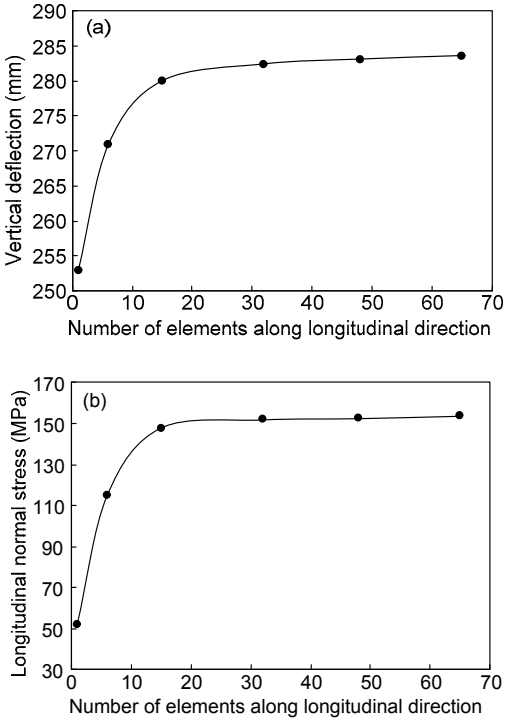


**Fig. 6 Variation of vertical deflections (a) and longitudinal normal stress (b) at the mid span as the elements increase**

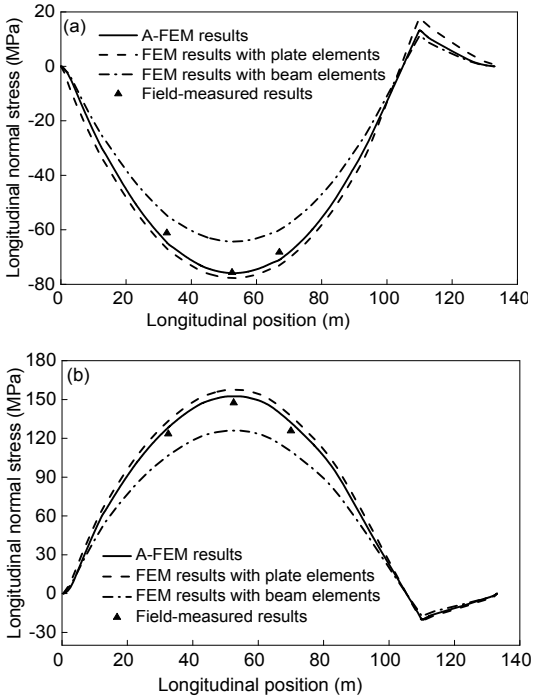


**Fig. 9 Comparison of longitudinal normal stress: (a) top edge; (b) bottom edge**

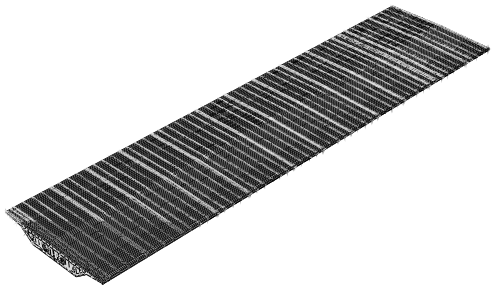

**Fig. 7 Plate element model of conventional FEM**

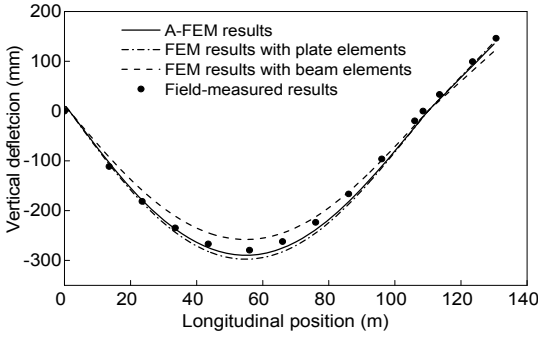


**Fig. 8 Comparison of vertical deflections**

**Table 1 Results of the maximum deflections and stresses**

| Method | Deflection (mm) | Stress of the top edge (MPa) | Stress of the bottom edge (MPa) |
|---|---|---|---|
| A-FEM | 281.1 | 73.8 | 152.5 |
| Conventional plate element | 284.6 | 76.1 | 157.5 |
| Conventional beam element | 258.9 | 64.9 | 125.8 |
| Field-measured data | 279.2 | 75.2 | 150.7 |

The results reveal that the deflections and stresses calculated by A-FEM are in good agreement with those of conventional plate elements and field-measured data, and the error is less than 2% for deflections and 5% for stresses. However, there is a great deviation using the beam element, where the error reaches 7.3% for deflections and 16.5% for stresses. Hence, the A-FEM meets the requirement of calculation precision when applied to practical complex spatial structures and significantly improves the computational efficiency.

## 4 Simulation and control of the construction process

Based on the A-FEM, the most adverse stress condition for each girder segment can be checked, and the construction parameters for prefabrication and erection can also be determined, such as the pre-camber of girder segments, the angle between two adjacent end-faces, the pre-set distance of the girder segments, and the effect of temperature difference. The predicted results prove to be accurate enough to ensure that the full-span erection can be carried out with good quality in a smooth manner.

### 4.1 Elevation control

One of the most important aspects of construction control is vertical elevation, where the pre-camber is the most critical parameter for elevation control of a girder segment. The manufacturing parameters in the unstressed state are determined based on the pre-camber to achieve the geometric shape in design ideal state. According to the specifications (MOT, 2015), the pre-camber $w_0$ is taken as the additive inverse of the sum for the cumulative deflections of girder segments during different construction stages and half of the deflection caused by the live load:

$$w_0 = -\left(\sum_{j=1}^{q} w_{gj} + 0.5w_v\right), \tag{10}$$

where $w_{gj}$ is the deflection produced in the $j$th construction stage, $w_v$ is the deflection caused by the live load, and $q$ is the number of construction stages.

Eq. (10) illustrates that it is important to accurately predict the vertical deflection of girder segments during each construction stage. Taking the periods after erecting the third segment and after erecting the final segment as two typical construction stages, Fig. 10 displays the cumulative vertical deflection of the girder during the two periods. The maximum deflection of the girder caused by the live load after erecting the final segment is displayed in Fig. 11. Fig. 12 shows the final vertical relative elevation of the girder considering the pre-camber. For comparison with the results of the A-FEM, the field-measured results during the erection of the girder segments are also presented in these figures.

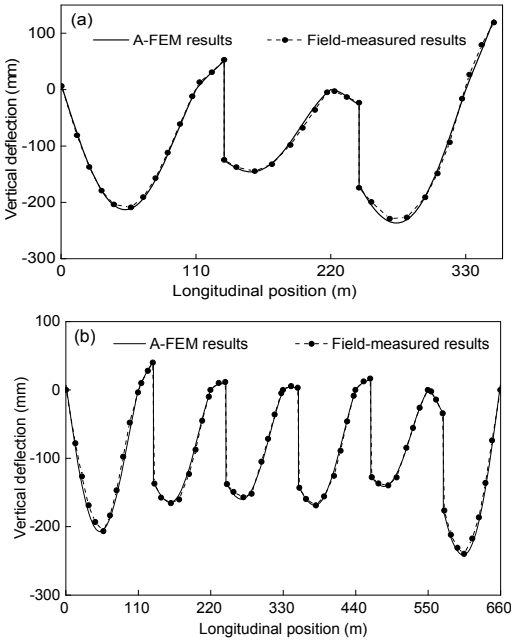


**Fig. 10 Cumulative vertical deflections of different construction stages after erecting the third segment (a) and after erecting the final segment (b)**

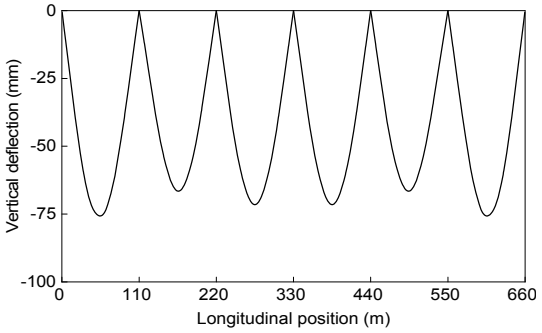


**Fig. 11 Maximum vertical deflections under live load**

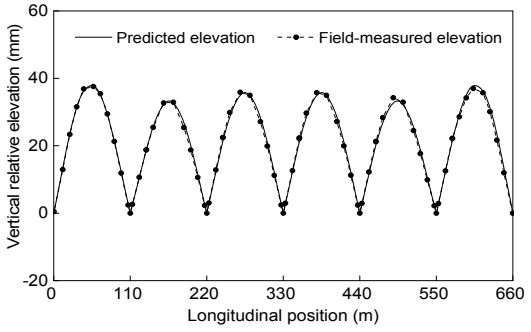


**Fig. 12 Final vertical relative elevation after construction**

The figures indicate that the field-measured results of each construction stage agree well with the predicted results based on the A-FEM, and the setting of pre-camber proves to be reasonable. The final vertical relative elevations of the girder after completion of construction based on the pre-camber predicted by A-FEM is consistent with the field-measured elevations in Fig. 12, and the errors of elevation are controlled within 10 mm. This fully meets the requirements of geometric accuracy for deck elevation.

### 4.2 Control of stress

The stress of a continuous steel box girder is changing constantly as construction progresses. In order to check the stress states of girder segments for safety, the stresses should be accurately predicted during their actual erection. For the verification of the predicted results, some measuring points were set on the girder segments, the positions of which were determined by the prediction of the most adverse stress state based on the A-FEM. Figs. 13a−13c show the comparison of measured and predicted results for the longitudinal distributions for normal stresses in the top and bottom edges of the girder under different erection stages and hoisting condition, respectively.

According to the A-FEM results, the location where the maximum normal stress occurs at the mid span, the top of piers, and the lifting point, are selected for monitoring. The field-measured results are close to the predicted values with 10% and 15% errors in erection and hoisting, respectively. Therefore, the stresses of the girder segments during their entire full-span erection can also be accurately predicted based on the A-FEM to assess structural safety.

### 4.3 Control for the end-face angle of the girder segments

During the full-span erection of a continuous steel girder, each girder segment should be smoothly connected after its elevation has been determined. Therefore, it is critical to control the angle between two adjacent end-faces of the girder segments. To control the maximum error of longitudinal distance between two adjacent end-faces of the girder segments within 2 mm before girth-welding, the angle of the two end-faces in the unstressed state must be set based on accurate calculation. As shown in Fig. 14, the end-face angle needs to be checked in three cases during the construction: (a) both segments are unstressed; (b) one segment is stressed and the other is unstressed; (c) both segments are stressed. The end-face angle in the unstressed state, $\theta_0$, can be expressed as

$$\theta_0=[(\Delta u_m^{\mathrm{b}}-\Delta u_m^{\mathrm{t}})+(\Delta u_m'^{\mathrm{b}}-\Delta u_m'^{\mathrm{t}})-(\Delta u_{m+1}'^{\mathrm{b}}-\Delta u_{m+1}'^{\mathrm{t}})]/h, \tag{11}$$

where $\Delta u_m^{\mathrm{t}}$ and $\Delta u_m^{\mathrm{b}}$ are the longitudinal displacements of the top and bottom edges at the end of segment $m$ during the $j$th construction stage, $\Delta u_m'^{\mathrm{t}}$,

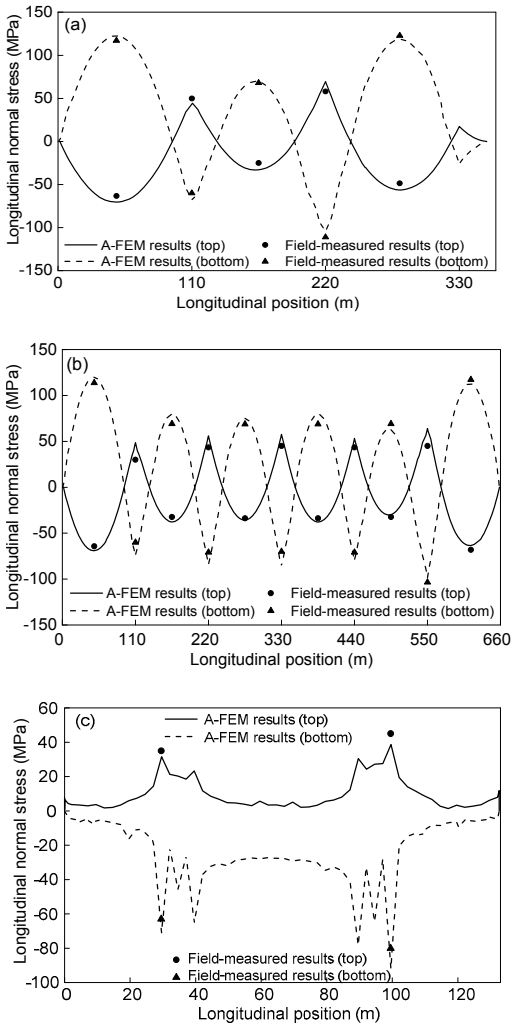


**Fig. 13 Longitudinal normal stress distributions under different construction stages of after erecting the intermediate segment (a) and after erecting the final segment (b), and under the hoisting condition (c)**

$\Delta u'^{\mathrm{b}}_m$, $\Delta u'^{\mathrm{t}}_{m+1}$, and $\Delta u'^{\mathrm{b}}_{m+1}$ are the longitudinal displacements of the top and bottom edges at the adjacent end-faces of segments $m$ and $m$+1 during the erection of the segment $m$+1, respectively, and $h$ is the depth of the girder. The construction parameters for controlling the end-face angle are listed in Table 2.

Before being erected, each pair of adjacent end-faces for the girder segments has been set a certain end-face angle in the unstressed state based on the data of Table 2. As a result, all the adjacent end-faces are kept parallel when being girth-welded at the construction site, indicating that the adjacent end-faces of girder segments can be perfectly matched by reasonably setting the end-face angles.

### 4.4 Control for locating accuracy in hoisting girder segments

The final states of a continuous steel box girder and its bearings are affected by the locating accuracy in hoisting the girder segment, which can be divided into three stages as shown in Fig. 15. When installing the permanent bearings, the girder segment is shifted from its initial position on the temporary bearings by a certain overall excursion. The relative offset between the top and bottom plates of the bearing can be counteracted by the longitudinal displacements of the bottom plate for the girder segment during remaining construction stages after the installation of permanent bearings. Therefore, the pre-set distance of the girder segment, $\delta$, can be derived as

$$\delta = -\sum_{j=1}^{q} u_j, \tag{12}$$

where $u_j$ is the longitudinal displacement at the bottom edge of the girder segment in the $j$th construction stage caused by gravity and thermal effect, the specified positive direction of which is consistent with the forward direction of construction.

When this method was applied to control the position accuracy in hoisting real girder segments, the field-measured eccentricities of bearings are less than 20 mm, indicating that the bearings were placed in the correct position without eccentric load under gravity and thermal effects, and the durability and safety of bearings were guaranteed.

**Table 2 Construction parameters for controlling the end-face angle**

| Position of the end-face angle | $\Delta u^{\mathrm{t}}_m$ (mm) | $\Delta u^{\mathrm{b}}_m$ (mm) | $\Delta u'^{\mathrm{t}}_m$ (mm) | $\Delta u'^{\mathrm{b}}_m$ (mm) | $\Delta u'^{\mathrm{t}}_{m+1}$ (mm) | $\Delta u'^{\mathrm{b}}_{m+1}$ (mm) | $\theta_0$ (°) |
|---|---|---|---|---|---|---|---|
| Segment 1-2 | 12.3 | −17.8 | −8.5 | 19.0 | −2.9 | 10.3 | −0.20 |
| Segment 2-3 | −1.2 | −25.9 | 1.4 | 29.9 | 7.7 | 20.4 | −0.11 |
| Segment 3-4 | 9.4 | −14.8 | 13.7 | 42.2 | 20.0 | 32.6 | −0.11 |
| Segment 4-5 | 21.7 | −2.6 | −4.8 | 24.4 | 1.7 | 14.5 | −0.10 |
| Segment 5-6 | 3.1 | −21.1 | 0.9 | 29.6 | 7.5 | 19.8 | −0.11 |

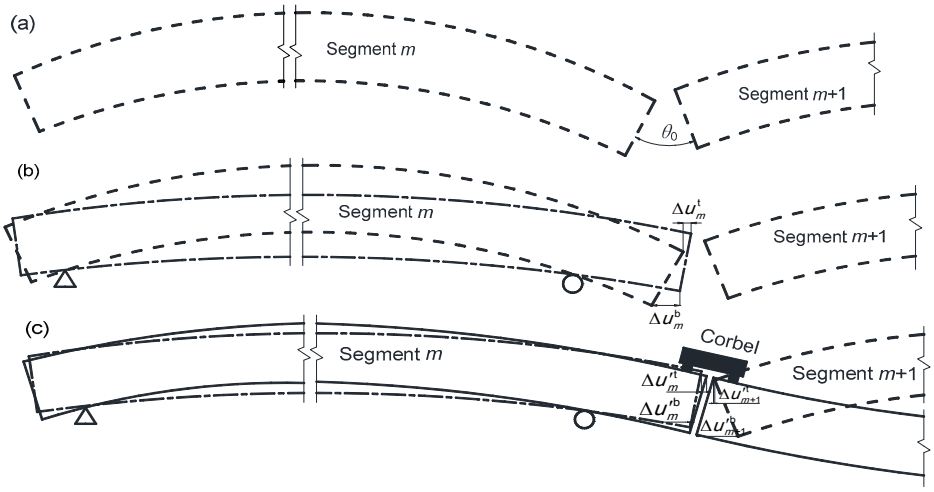


**Fig. 14 Different states of the end-face angle between adjacent segments: (a) unstressed state; (b) intermediate state which is stressed on the left and unstressed on the right; (c) installed state**

### 4.5 Evaluation for the effect of temperature difference

The deflections and stresses of the full-span girder segments are affected markedly by the vertical temperature difference effect, which must be accurately predicted and evaluated to ensure the safety of the bridge and correct position of each segment during construction. Figs. 16 and 17 compare the longitudinal distribution of the simulated deflections and stresses with that of the field-measured results under different temperature differences.

The deflections and stresses under each temperature difference calculated by A-FEM are in accordance with those measured in-situ. When the temperature difference reaches the maximum value of 14.5 °C, the deflections at the mid span and cantilever are 65.5 mm and −70.6 mm, respectively. Under these positive temperature differences, the stress increment at the top edge of the girder segment is more obvious than that at the bottom edge, with a maximum of 38.5 MPa. Even if the temperature difference was only 2.5 °C, there would have been already obvious thermal deflections of the girder segment. Therefore, the temperature difference between top and bottom plates should be strictly controlled before segments are erected and welded.

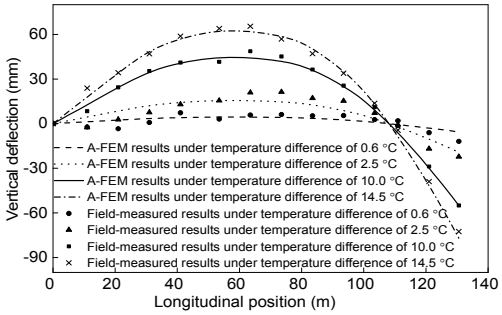


**Fig. 16 Vertical deflections induced by temperature differences between top and bottom edges**

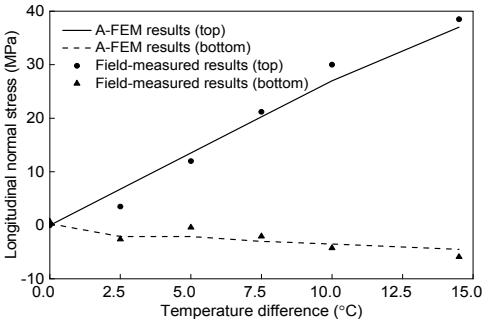


**Fig. 17 Normal stress at the mid span under different temperature differences**

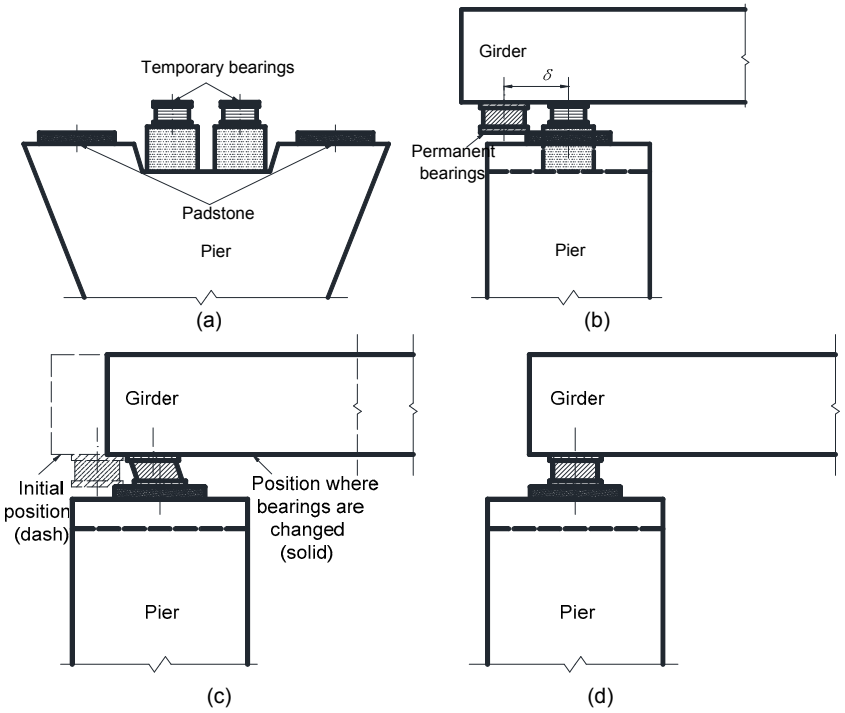


**Fig. 15 Process of locating the segment: (a) arrangement of temporary bearings; (b) initial state; (c) position where temporary bearings are changed to permanent bearings; (d) final state when the bridge is completed**

## 5 Conclusions

Based on the separation of mathematical and physical meshes, the A-FEM is more efficient than the conventional FEM. Verified by the field-measured data, its accuracy has met engineering requirements, and can be applied to the refined analysis for the construction process of complex long-span bridges.

Based on the A-FEM results for the deflections and stress of each construction stage, the elevation of girder segments for erection can be precisely controlled, and the most adverse load positions can be identified and checked. The end-face angles between adjacent girder segments in their unstressed states are determined by analyzing the displacements of the nodes at the end of segments to ensure a smooth connection during construction. The pre-set distance of the girder segment is precisely set to ensure that bearings are still in the specified position under gravity and thermal loads. The effects of temperature difference on girder segments are evaluated by calculating girder deflections and stresses under different temperature differences. By controlling these key parameters, the full-span erection of a continuous steel box girder can be effectively guided.

### Contributors

Jin-feng WANG designed the research. Tian-mei WU processed the corresponding data and wrote the first draft of the manuscript. Jin-feng WANG, Jiang-tao ZHANG, and Hua-wei XIANG helped to organize the manuscript. Jin-feng WANG and Rong-qiao XU revised and edited the final version.

### Conflict of interest

Jin-feng WANG, Tian-mei WU, Jiang-tao ZHANG, Hua-wei XIANG, and Rong-qiao XU declare that they have no conflict of interest.

### References

Fang XJ, Yang QD, Cox BN, et al., 2011. An augmented cohesive zone element for arbitrary crack coalescence and bifurcation in heterogeneous materials. *International Journal for Numerical Methods in Engineering*, 88(9): 841-861. https://doi.org/10.1002/nme.3200

Huang W, 2007. Design of deck pavement for long-span steel bridges. *China Civil Engineering Journal*, 40(9):65-77 (in Chinese). https://doi.org/10.15951/j.tmgcxb.2007.09.004

Jung J, Do BC, Yang QD, 2016. Augmented finite-element method for arbitrary cracking and crack interaction in solids under thermo-mechanical loadings. *Philosophical Transactions of the Royal Society A: Mathematical, Physical and Engineering Sciences*, 374(2071): 20150282. https://doi.org/10.1098/rsta.2015.0282

Lee KM, Cho HN, Cha CJ, 2006. Life-cycle cost-effective optimum design of steel bridges considering environmental stressors. *Engineering Structures*, 28(9):1252-1265. https://doi.org/10.1016/j.engstruct.2005.12.008

Ling DS, Yang QD, Cox B, 2009. An augmented finite element method for modeling arbitrary discontinuities in composite materials. *International Journal of Fracture*, 156(1):53-73. https://doi.org/10.1007/s10704-009-9347-2

Ling DS, Tu FB, Bu LF, 2012. Enhanced finite element analysis of progressive failure of slopes based on cohesive zone model. *Chinese Journal of Geotechnical Engineering*, 34(8):1387-1393 (in Chinese).

Ling DS, Bu LF, Tu FB, et al., 2014. A finite element method with mesh-separation-based approximation technique and its application in modeling crack propagation with adaptive mesh refinement. *International Journal for Numerical Methods in Engineering*, 99(7):487-521. https://doi.org/10.1002/nme.4689

Liu W, Yang QD, Mohammadizadeh S, et al., 2013. An accurate and efficient augmented finite element method for arbitrary crack interactions. *Journal of Applied Mechanics*, 80(4):041033. https://doi.org/10.1115/1.4007970

Liu Y, Yang CX, Tan ZC, 2017. Hybrid element-based virtual distortion method for finite element model updating of bridges with wide-box girders. *Engineering Structures*, 143:558-570. https://doi.org/10.1016/j.engstruct.2017.04.030

MOT (Ministry of Transport of the People's Republic of China), 2015. Specifications for Design of Highway Steel Bridges, JTG D64-2015. National Standards of the People's Republic of China (in Chinese).

Naderi M, Jung J, Yang QD, 2016. A three dimensional augmented finite element for modeling arbitrary cracking in solids. *International Journal of Fracture*, 197(2):147-168. https://doi.org/10.1007/s10704-016-0072-3

Nguyen TT, Kim NI, Lee J, 2016. Analysis of thin-walled open-section beams with functionally graded materials. *Composite Structures*, 138:75-83. https://doi.org/10.1016/j.compstruct.2015.11.052

Prokić A, 1993. Thin-walled beams with open and closed cross-sections. *Computers & Structures*, 47(6):1065-1070. https://doi.org/10.1016/0045-7949(93)90310-A

Razaqpur AG, Li HG, 1991. Thin-walled multicell box-girder finite element. *Journal of Structural Engineering*, 117(10):2953-2971. https://doi.org/10.1061/(asce)0733-9445(1991)117:10(2953)

Sapountzakis EJ, Dikaros IC, 2019. Advanced 3-D beam element including warping and distortional effects for the analysis of spatial framed structures. *Engineering Structures*, 188:147-164. https://doi.org/10.1016/j.engstruct.2019.03.006

Su QK, Xie HB, 2016. Summary of steel bridge construction of Hong Kong-Zhuhai-Macao Bridge. *China Journal of Highway and Transport*, 29(12):1-9 (in Chinese). https://doi.org/10.19721/j.cnki.1001-7372.2016.12.001

Thang DD, Koo MS, Hameed A, 2009. Optimum cost design of steel box-girder by varying plate thickness. *KSCE Journal of Civil Engineering*, 13(1):31-37. https://doi.org/10.1007/s12205-009-0031-x

Vu QV, Thai DK, Kim SE, 2018. Effect of intermediate diaphragms on the load–carrying capacity of steel–concrete composite box girder bridges. *Thin-Walled Structures*, 122:230-241. https://doi.org/10.1016/j.tws.2017.10.024

Wu YP, Zhu YL, Lai YM, et al., 2002. Analysis of shear lag and shear deformation effects in laminated composite box beams under bending loads. *Composite Structures*, 55(2):147-156. https://doi.org/10.1016/S0263-8223(01)00138-6

Wu GF, Xu H, 2005. Theoretical and experimental study on shear lag effect of partially cable-stayed bridge. *Journal of Zhejiang University-SCIENCE*, 6A(8):875-877. https://doi.org/10.1631/jzus.2005.A0875

## 中文概要

**题　目：** 大悬臂连续钢箱梁桥整孔安装的精细化分析及施工参数计算

**目　的：** 以港珠澳大桥连续钢箱梁桥为工程背景，探究适用于模拟全桥全施工阶段且具有高精度的空间有限元方法，并分析整孔安装的关键施工参数，从而高效准确地控制大型复杂桥梁结构的整孔安装精度。

**创新点：** 1. 采用基于网格分离的空间强化有限元法，能够在保证精度的同时简化复杂结构的网格剖分问题，且适用于任意边界、构造及荷载的空间分析。2. 在三维实体单元的基础上引入退化板单元，并对不同物理单元的本构关系矩阵进行修正，使其适用于薄壁结构分析。3. 精确计算施工控制参数，以有效地指导连续钢箱梁的整孔安装过程。

**方　法：** 1. 采用空间强化有限元法，并引入退化板单元，对连续钢箱梁桥进行全桥全施工阶段分析。2. 基于结构响应，计算相邻节段间的端面转角、节段预偏距和温差效应等关键参数以控制整孔安装施工精度，并与传统有限元法及工程实测数据进行对比验证。

**结　论：** 1. 相较于传统有限元法，空间强化有限元法更高效，且其精度满足工程要求。2. 根据各施工阶段的结构响应，可以精确地控制梁段高程，以及识别和校核最不利荷载位置。3. 精确地控制相邻节段在无应力状态下的端部转角、梁段预偏距和箱梁顶底板温差等施工参数，能够使梁段平顺连接，使最终支座处于正位状态，并避免温差效应的影响，从而实现对整孔安装施工的高精度控制。

**关键词：** 连续钢箱梁桥；整孔安装；强化有限元；施工控制；施工参数计算